01 Jan 2006

Effects of Current on Droplet Generation and Arc Plasma in Gas Metal Arc Welding

J. Hu

Hai-Lung Tsai
Missouri University of Science and Technology, tsai@mst.edu

Effects of current on droplet generation and arc plasma in gas metal arc welding

J. Hu[a)] and H. L. Tsai[b)]

Department of Mechanical and Aerospace Engineering, University of Missouri-Rolla, 1870 Miner Circle, Rolla, Missouri 65409

In gas metal arc welding (GMAW), a technology using pulsed currents has been employed to achieve the one-droplet-per-pulse (ODPP) metal transfer mode with the advantages of low average currents, a stable and controllable droplet generation, and reduced spatter. In this paper, a comprehensive model was developed to study the effects of different current profiles on the droplet formation, plasma generation, metal transfer, and weld pool dynamics in GMAW. Five types of welding currents were studied, including two constant currents and three wave form currents. In each type, the transient temperature and velocity distributions of the arc plasma and the molten metal, and the shapes of the droplet and the weld pool were calculated. The results showed that a higher current generates smaller droplets, higher droplet frequency, and higher electromagnetic force that becomes the dominant factor detaching the droplet from the electrode tip. The model has demonstrated that a stable ODPP metal transfer mode can be achieved by choosing a current with proper wave form for given welding conditions. © *2006 American Institute of Physics.*
[DOI: 10.1063/1.2337261]

I. INTRODUCTION

In gas metal arc welding (GMAW), current is one of the most important factors affecting the mode of metal transfer and subsequently the weld quality. At low currents, the globular transfer mode occurs with large droplets formed at the tip of the electrode and then detached at a rate of only several droplets per second. In the spray transfer mode at high currents, droplets are formed at the frequency that can be up to several hundreds per second and have a diameter smaller than the diameter of the electrode. The dynamics of droplet formation and the transition from globular transfer mode to spray transfer mode are determined by the combined effect of various forces acting on the droplet. These forces include surface tension, electromagnetic force, gravity, arc pressure, and plasma shear stress due to the flow of arc plasma around the droplet at the tip of the electrode. Surface tension force is the major attaching force that tries to hold the droplet to the electrode, especially at low currents. The magnitudes of electromagnetic force, arc pressure, and plasma shear stress increase as current increases and the combined effect of these three forces is to detach the droplet from electrode. At high currents, the detaching effect of electromagnetic force acting on the droplet becomes dominant and small droplets are detached from the electrode.

The globular transfer mode causes significant spatters and has poor welding quality,[1] while the spray transfer mode has regular droplet detachment, directional droplet transfer, and low spatters.[2] However, spray transfer can only be achieved at high currents, which lead to a big weld pool and thus a big heat-affected zone, which is not suitable for heat-sensitive materials. Recently, a technology using pulsed currents has been employed to achieve the one-droplet-per-pulse[3] (ODPP) metal transfer mode with the advantages of low average currents, a stable and controllable droplet generation, and reduced spatter. Obtaining a ODPP transfer mode requires a set of "correct" pulse parameters, including peak current (I_p) and its duration (t_p), and base current (I_b) and its duration (t_b), as illustrated in Fig. 1. The peak and base durations also define the pulse frequency and welding duty cycle. In addition, the wire feed rate must be correctly set to match the burn-off rate that is closely related to the pulse parameters. However, so far the ODPP technology has been developed by the trial-and-error procedure which is not only very time consuming and costly but also very difficult to obtain optimum welding conditions.

Many models[3–17] have been developed to study the metal transfer process. Typical approaches include the static force balance theory (SFBT),[4–6] the pinch instability theory (PIT),[3,7,8] and the volume of fluid (VOF) method.[9–17] By considering the effects of surface tension, gravity, and electromagnetic force, these models were able to predict the metal transfer frequency or the droplet shape. However, the heat transfer, phase change, and the coupling with arc plasma were ignored in these models. In fact, the heat transfer and phase-change effects are very important to determine the electrode melting interface and the droplet generation rate,
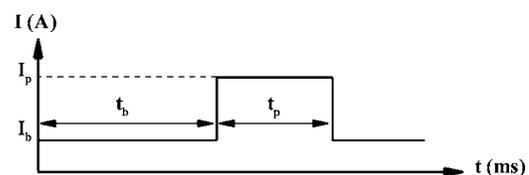
a)Present address: Department of Mechanical Engineering, University of Bridgeport, Bridgeport, CT 06604.
b)FAX: +1-573-341-4607; electronic mail: tsai@umr.edu

FIG. 1. Current wave form for pulsed GMAW.
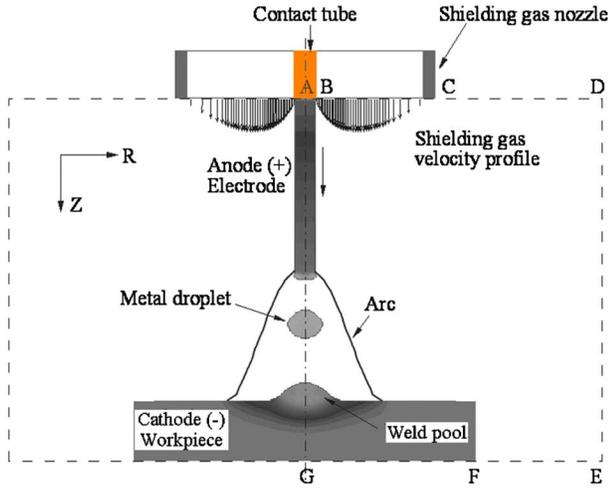
100, 053304-1

FIG. 2. A schematic representation of a GMAW system including the electrode, the arc, and the weld pool (not to scale).

and thus have significant impacts on the metal transfer mode. The coupling of arc plasma with metal can provide more accurate current distributions in both the arc plasma and the metal, the heat transfer across the arc-metal interface, the arc plasma shear stress, and arc pressure at the metal surface.

In this paper, a comprehensive model is developed to simulate the transient, coupled transport phenomena occurring during the gas metal arc welding process. This includes the arc plasma, melting of the electrode, droplet formation, detachment, transfer, and impingement onto the workpiece, and weld pool fluid flow and dynamics. Using this comprehensive model, simulations were performed under two constant currents and three pulsed currents to study the effects of current on droplet formation, detachment, and weld pool dynamics.

II. MATHEMATICAL MODEL

A. Governing equations

Figure 2 is a schematic sketch of a stationary axisymmetric GMAW system. In this system, a current is applied to the electrode through the contact tube at the top of the computational domain. An arc plasma is struck between the electrode and the workpiece. The electrode is continuously fed downward and then melted at the tip by the high temperature arc. Droplets are formed at the molten electrode tip and are then detached and transferred to the workpiece. A weld pool is formed by the continuous impingement of droplets and dynamic interactions with the high temperature and high pressure arc plasmas at the workpiece. Inert shielding gas is provided through the shielding gas nozzle to prevent the molten metal from oxidation.

The computational domain has an anode region, an arc region, and a cathode region. For GMAW, the anode region is the electrode, and the cathode region is the workpiece. The differential equations governing the arc, the electrode, and the workpiece can be put into a single set. The differential equations governing the conservation of mass, momentum, and energy based on the continuum formulation given by Diao and Tsai[18] are modified and employed in the present

study, and the current continuity equation is used to calculate the current density distribution. The equations are given below.

(1) Mass continuity,

$$\frac{\partial}{\partial t}(\rho) + \nabla \cdot (\rho \mathbf{V}) = 0 \tag{1}$$

(2) Momentum,

$$\frac{\partial}{\partial t}(\rho u) + \nabla \cdot (\rho \mathbf{V} u) = \nabla \cdot \left(\mu_l \frac{\rho}{\rho_l} \nabla u \right) - \frac{\partial p}{\partial r} - \frac{\mu_l}{K} \frac{\rho}{\rho_l} (u - u_s)$$
$$- \frac{C\rho^2}{K^{1/2}\rho_l} |u - u_s|(u - u_s)$$
$$- \nabla \cdot (\rho f_s f_l \mathbf{V}_r u_r) - J_z B_\theta, \tag{2}$$

$$\frac{\partial}{\partial t}(\rho v) + \nabla \cdot (\rho \mathbf{V} v) = \nabla \cdot \left(\mu_l \frac{\rho}{\rho_l} \nabla v \right) - \frac{\partial p}{\partial z} - \frac{\mu_l}{K} \frac{\rho}{\rho_l} (v - v_s)$$
$$- \frac{C\rho^2}{K^{1/2}\rho_l} |v - v_s|(v - v_s)$$
$$- \nabla \cdot (\rho f_s f_l \mathbf{V}_r v_r) + \rho g \beta_T (T - T_0)$$
$$+ J_r B_\theta. \tag{3}$$

(3) Energy,

$$\frac{\partial}{\partial t}(\rho h) + \nabla \cdot (\rho \mathbf{V} h) = \nabla \cdot \left(\frac{k}{c_s} \nabla h \right) + \nabla \cdot \left(\frac{k}{c_s} \nabla (h_s - h) \right)$$
$$- \nabla \cdot [\rho (\mathbf{V} - \mathbf{V}_s)(h_l - h)]$$
$$- \Delta H \frac{\partial f_l}{\partial t} + \frac{J_r^2 + J_z^2}{\sigma_e} - S_R$$
$$+ \frac{5k_b}{e} \left(\frac{J_r}{c_s} \frac{\partial h}{\partial r} + \frac{J_z}{c_s} \frac{\partial h}{\partial z} \right). \tag{4}$$

(4) Current continuity,

$$\nabla^2 \phi = \frac{1}{r} \frac{\partial}{\partial r} \left(r \frac{\partial \phi}{\partial r} \right) + \frac{\partial^2 \phi}{\partial z^2} = 0. \tag{5}$$

(5) Ohm's law,

$$J_r = -\sigma_e \frac{\partial \phi}{\partial r}, \quad J_z = -\sigma_e \frac{\partial \phi}{\partial z}. \tag{6}$$

(6) Maxwell's equation,

$$B_\theta = \frac{\mu_0}{r} \int_0^r J_z r \, dr. \tag{7}$$

In Eqs. (1)–(4), u and v are the velocities in the r and z directions, respectively. $\mathbf{V}_r = (\mathbf{V}_l - \mathbf{V}_s)$ is the relative velocity vector between the liquid phase and the solid phase in the mushy zone. The subscripts s and l refer to the solid and liquid phases, respectively, and the subscript 0 represents the initial condition. p is the pressure, T is the temperature, h is the enthalpy, ϕ is the electrical potential, ρ is the density, μ is the viscosity, k is the thermal conductivity, g is the gravitational acceleration, β_T is the thermal expansion coefficient, c is the specific heat, σ_e is the electrical conductivity, J_r and

J_z are current densities in the respective r and z directions, B_θ is the self-induced electromagnetic field, S_R is the radiation heat loss, μ_0 is the magnetic permeability, k_b is the Stefan-Boltzmann constant, and e is the electronic charge.

The third and fourth terms on the right-hand side of Eqs. (2) and (3) represent the respective first- and second-order drag forces for the flow in the mushy zone. The fifth term on the right-hand side of Eqs. (2) and (3) represents an interaction between the solid and the liquid phases. The second term on the right-hand side of Eq. (4) represents the net Fourier diffusion flux. While the third term represents the energy flux associated with the relative phase motion, and the fourth term is used to consider the latent heat of fusion. All the terms mentioned in this paragraph are zero, except in the mushy zone. When Eqs. (2)–(4) are used to calculate the arc plasma, these terms associated with the mushy zone are set to zero and all the thermal physical properties are replaced with those of the arc plasma. In the present study, for metal domain calculations, the solid phase velocity is assumed to be zero due to a relative small weld pool (as compared to, for example, a casting), concentrated arc heat, and rapid solidification of the weld pool after the arc is turned off.

The second-to-last term on the right-hand side of Eq. (3) is the thermal expansion term. The last term of Eqs. (2) and (3) is the electromagnetic force term. The last three terms in Eq. (4) are Ohmic heating, radiation loss, and electron enthalpy flow, respectively.

Continuum density ρ, specific heat c, thermal conductivity k, solid mass fraction f_s, liquid mass fraction f_l, velocity V, and enthalpy h are defined as follows:

$$\rho = g_s\rho_s + g_l\rho_l, \quad c = f_sc_s + f_lc_l, \quad k = g_sk_s + g_lk_l,$$

$$f_s = \frac{g_s\rho_s}{\rho}, \quad f_l = \frac{g_l\rho_l}{\rho},$$

$$V = f_sV_s + f_lV_l, \quad h = h_sf_s + h_lf_l, \tag{8}$$

where g_s and g_l are the solid volume fraction and liquid volume fraction. Assuming constant phase specific heats, the phase enthalpy for the solid and liquid can be expressed as

$$h_s = c_sT, \quad h_l = c_lT + (c_s - c_l)T_s + H, \tag{9}$$

where H is the latent heat of fusion for the alloy.

The assumption of permeability function in the mushy zone requires consideration of the growth morphology specific to the alloy under study. In the present study, the permeability function analogous to fluid flow in porous media is assumed, employing the Carman-Kozeny equation[19,20]

$$K = \frac{g_l^3}{c_1(1 - g_l)^2}, \quad c_1 = \frac{180}{d^2}, \tag{10}$$

where d is proportional to the dendrite dimension, which is assumed to be a constant and is on the order of 10^{-2} cm. The inertial coefficient C can be calculated from[21]

$$C = 0.13g_l^{-3/2}. \tag{11}$$

B. Arc region

In the arc region, the plasma is assumed to be in local thermodynamic equilibrium (LTE),[22] implying that the electron and the heavy particle temperatures are equal. On this basis, the plasma properties, including enthalpy, specific heat, density, viscosity, thermal conductivity, and electrical conductivity, are determined from an equilibrium composition calculation.[22] It is noted that the metal vaporized from the metal surface may influence plasma material properties, but this effect is omitted in the present study. It is also assumed that the plasma is optically thin, thus the radiation may be modeled in an approximate manner by defining a radiation heat loss per unit volume.[22]

C. Anode sheath region

At the plasma-electrode interface, there exists an anode sheath region.[22] In this region, the mixture of plasma and metal vapor departs from LTE, thus it no longer complies with the model presented above. The anode sheath region has been neglected in many arc models,[9,23–25] which leads to a more constricted arc distribution at the bottom of the droplet. This paper adopts the anode sheath the formulation of Haidar[26] by including a noncollisional sheath region for the anode. Formulation of the noncollisional zone is based on the Langmuir sheath model. Heat transfer from the plasma to the electrode is determined by charged particle fluxes across the sheath. These fluxes are due to the electrons and the ions from the plasma, and also to a limited number of electrons emitted from the anode surface due to the thermionic emission. The corresponding current densities of these electrons and ions flow are J_e, J_i, and J_R. As J_R is several orders of magnitude lower than J_e and J_i, it is omitted in the calculation for simplification. The following formulations[26] are used to calculate the anode voltage drop across the sheath V_s:

$$J = J_e - J_i,$$

$$J_e = en_{e,s}\left(\frac{k_bT_{e,s}}{2\pi m_e}\right)^{0.5}\exp\left(\frac{eV_s}{k_bT_{e,s}}\right),$$

$$J_i = \tfrac{1}{4}en_{e,s}v_B,$$

$$V_s \leq 0, \tag{12}$$

where J is the total current density at the arc-anode interface calculated from the current density equation (5), J_i and J_e are calculated from the electron number density as charge neutrality is assumed valid through the transition zone, $T_{e,s}$ is the electron temperature at the sheath edge, which is taken as the local plasma temperature calculated from LTE, $n_{e,s}$ is the electron number density at the sheath edge, which is taken as the equilibrium electron number density at the local plasma temperature, v_B is the Bohm velocity given by $v_B = (k_bT_{e,s}/m_i)^{0.5}$, e is the electronic charge, k_b is the Stefan-Boltzmann constant, m_e is the electron mass, and m_i is the ion mass for the plasma gas.

The energy balance equation at the anode surface is modified to include a source term S_a expressing the heating

effects due to conduction by neutral particles, charge transport across the sheath through J_e and J_i, and cooling effects due to evaporation and blackbody radiation,

$$S_a = \frac{k_{\text{eff}}(T_{e,s} - T_a)}{\delta} + J_i\left(V_i - V_s + \frac{5k_b}{2e}T_a\right)$$
$$+ J_e\left(\phi_w + \frac{5k_b}{2e}T_{e,s}\right) - q_{\text{ev}}H_{\text{ev}} - \varepsilon k_b T_a^4, \tag{13}$$

where k_{eff} is the thermal conductivity taken at the arc plasma temperature, T_a is the anode surface temperature, δ is the length of the anode sheath region and the maximum experimentally observed thickness of the anode fall region is 0.1 mm,[27] V_i is the ionization energy of the plasma gas, ϕ_w is the work function of the anode material, ε is the emissivity of the surface, q_{ev} is the evaporation mass rate of metal vapor, and H_{ev} is the latent heat of vaporization. For metal such as steel, q_{ev} can be written as[28]

$$\log(q_{\text{ev}}) = A_v + \log P_{\text{atm}} - 0.5\log T, \tag{14}$$

$$\log P_{\text{atm}} = 6.121 - \frac{18\,836}{T}. \tag{15}$$

The energy balance equation for the plasma in the transition zone is also modified to include a source term S_{ap} expressing the cooling effects due to conduction by neutral particles and charge transport across the sheath through J_e and J_i,

$$S_{\text{ap}} = -\frac{k_{\text{eff}}(T_{e,s} - T_a)}{\delta} - J_i\left(V_i + \frac{5k_b}{2e}T_a\right)$$
$$- J_e\left(\frac{5k_b}{2e}T_{e,s} - V_s\right). \tag{16}$$

D. Cathode sheath region

Similar to the anode region, there exists a cathode sheath region between the plasma and the cathode. However, the physics of the cathode sheath and the energy balance at the nonthermionic cathode for GMAW are not well understood.[3,9,10] The thermal effect due to the cathode sheath has been omitted in many models but reasonable results were obtained.[9,10] Thus, the source term of the energy balance equation at the cathode surface will only consider conduction, radiation, and evaporation,

$$S_c = \frac{k_{\text{eff}}(T_{\text{arc}} - T_c)}{\delta} - q_{\text{ev}}H_{\text{ev}} - \varepsilon k_b T_c^4, \tag{17}$$

where k_{eff} is the effective thermal conductivity at the arc-cathode surface taken as the thermal conductivity of the arc plasma, δ is the length of the cathode sheath region, and T_c is the cathode surface temperature.

In additional to the heat loss by conduction, another positive term is included in the energy source term for the plasma at the cathode surface. This positive term is used to approximate the energy used in the cathode boundary layer to ionize the plasma[29] and it can also eliminate the unreason-

able cooling effect of the electron flow term in the cathode region.[22] The energy source term for the plasma at the cathode surface is given by

$$S_{\text{cp}} = -\frac{k_{\text{eff}}(T_{\text{arc}} - T_c)}{\delta} + \frac{5k_b(T_{\text{arc}} - T_c)}{2e}. \tag{18}$$

E. Metal region (electrode, droplet, and workpiece)

In this model, the anode region and cathode region change their shapes with time. Together with free droplets in the arc, they consist of the metal region, which is occupied by metal. The temperature distribution within the metal region is at an energy balance of conduction, Ohmic heating, and convection in the metal and the heat transferred from the arc plasma. Considerations are also given to energy gains and losses due to latent heat resulting from melting and solidification at the solid-liquid interface. Changes in the shape of the electrode tip and the weld pool surface result in changes in the current distribution, the heat generated due to Ohmic heating, and the heat transferred from the arc to the metal surface.

F. Tracking of solid-liquid interface

The solid/liquid phase-change boundary is handled by the continuum model.[18] The third, fourth, and fifth terms on the right-hand side of Eqs. (2) and (3) vanish at the solid phase because $u = u_s = v = v_s = 0$ and $f_l = 0$. For the liquid region, since K goes to infinity due to $g_l = 1$ in Eq. (10) and $f_s = 0$, all the aforementioned terms also vanish. These terms are only valid in the mushy zone, where $0 < f_l < 1$ and $0 < f_s < 1$. Therefore, there is no need to explicitly track the phase-change boundaries, and the liquid region, mushy zone, and solid region all are calculated by Eqs. (2) and (3). During the fusion and solidification processes, the latent heat is absorbed or released in the mushy zone, which is handled through the use of enthalpy defined in Eq. (9).

G. Tracking of free surfaces

Precise tracking of the free surface of the droplet and the welding pool are essential to correctly predict the shape of the droplet and the weld pool as a function of time. The algorithm of VOF is used to track the moving free surface.[30] The fluid configuration is defined by a volume of fluid function, $F(r, z, t)$, which tracks the location of the free surface. This function represents the volume of fluid per unit volume and satisfies the following conservation equation

$$\frac{dF}{dt} = \frac{\partial F}{\partial t} + (\boldsymbol{V} \cdot \nabla)F = 0. \tag{19}$$

When averaged over the cells of a computing mesh, the average value of F in a cell is equal to the fractional volume of the cell occupied by the metal. A unit value of F corresponds to a cell full of metal, whereas a zero value indicates that the cell contains no metal. Cells with F values between zero and one are partially filled with metal.

TABLE I. Boundary conditions on the outer boundaries.

	AB	BC	CD	DE	EF	FG	GA
u	0	0	0	$\dfrac{\partial(\rho u)}{\partial r}=0$	0	0	0
v	v_w	Eq. (25)	$\dfrac{\partial(\rho v)}{\partial z}=0$	0	0	0	$\dfrac{\partial v}{\partial r}=0$
h	$T=300$ K	$T=300$ K	$T=300$ K	$T=300$ K	$T=300$ K	$T=300$ K	$\dfrac{\partial T}{\partial r}=0$
ϕ	$-\sigma\dfrac{\partial\phi}{\partial z}=\dfrac{I}{\pi R_c^2}$	$\dfrac{\partial\phi}{\partial z}=0$	$\dfrac{\partial\phi}{\partial z}=0$	$\dfrac{\partial\phi}{\partial r}=0$	$\phi=0$	$\phi=0$	$\dfrac{\partial\phi}{\partial r}=0$

H. Forces at the arc plasma and metal interface

The molten part of the metal is subjected to body forces such as gravity and electromagnetic force. It is also subjected to surface forces such as surface tension due to surface curvature, Marangoni shear stress due to temperature difference, and arc plasma shear stress and arc pressure at the arc plasma and metal interface. For cells containing a free surface, surface tension pressure normal to the free surface can be expressed as[30]

$$p_s = \gamma\kappa, \tag{20}$$

where γ is the surface tension coefficient and κ is the free surface curvature given by

$$\kappa = -\left[\nabla\cdot\left(\frac{\mathbf{n}}{|\mathbf{n}|}\right)\right] = \frac{1}{|\mathbf{n}|}\left[\left(\frac{\mathbf{n}}{|\mathbf{n}|}\cdot\nabla\right)|\mathbf{n}| - (\nabla\cdot\mathbf{n})\right], \tag{21}$$

where $\mathbf{n}$ is a vector normal to the local free surface which equals the gradient of the VOF function

$$\mathbf{n} = \nabla F. \tag{22}$$

The temperature-dependent Marangoni shear stress at the free surface in a direction tangential to the local free surface is given by[16]

$$\tau_{\text{Ms}} = \frac{\partial\gamma}{\partial T}\frac{\partial T}{\partial\mathbf{s}}, \tag{23}$$

where $\mathbf{s}$ is a vector tangential to the local free surface.

The arc plasma shear stress is calculated at the free surface from the velocities of arc plasma cells immediately adjacent the metal cells,

$$\tau_{\text{ps}} = \mu\frac{\partial\mathbf{V}}{\partial\mathbf{s}}, \tag{24}$$

where μ is the viscosity of arc plasma.

The arc pressure at the metal surface is obtained from the computational result in the arc region. The surface forces are included by adding source terms to the momentum equations according to the continuum surface force (CSF) model.[30] Using F of the VOF function as the characteristic function, the surface tension pressure, Marangoni shear stress, arc plasma shear stress, and arc pressure are all trans-

formed to the localized body forces and added to the momentum transport equations as source terms at the boundary cells.

I. Boundary conditions

1. External boundary conditions

The calculation domain, as shown in Fig. 2, is *ABCDEFGA*. Only half of the entire physical domain is calculated due to the cylindrical symmetry along the centerline *AG*. The corresponding external boundary conditions for the entire domain are listed in Table I. Symmetrical boundary conditions are used along the centerline *AG*. The wire feed rate is incorporated through a boundary condition on v along *AB*. The imposed shielding gas flow is set through a boundary condition on v along *BC*. For the inflow of gas from the nozzle, the radial velocity component is omitted and the axial velocity component is determined from the formula for pipe flow as shown in the following:[31]

$$v(r) = \frac{2Q}{\pi}\frac{\{R_n^2 - r^2 + (R_n^2 - R_w^2)[\ln(r/R_n)/\ln(R_n/R_w)]\}}{\{R_n^4 - R_w^4 + [(R_n^2 - R_w^2)^2/\ln(R_n/R_w)]\}}$$
$$+ V_w\frac{\ln R_n/r}{\ln R_n/R_w}, \tag{25}$$

where Q is the inflow rate of the shielding gas, R_w is the radius of the electrode, R_n is the internal radius of the shielding gas nozzle, and V_w is the wire feed rate. A constant mass flow boundary condition is used for the open boundaries *CD* and *DE*.

The temperature boundaries along *AD*, *DE*, and *EG* are determined by the ambient condition, which is set as room temperature, 300 K. Uniform current density is specified along *AB* as $J_z = -\sigma_e(\partial\phi/\partial z) = I/\pi R_w^2$. The voltage ϕ is set to zero at the bottom of the workpiece *FG*.

2. Internal boundary conditions

Within the computational domain, the moving surface of the electrode, droplet, and weld pool forms a moving inner boundary condition for the arc region. VOF, Eq. (19), is solved in the metal domain to track the moving free surface with free boundary conditions set at the metal free surface.

Additional body force source terms are added to the momentum transport equations at the metal free surface to consider the effects of surface tension, Maragoni shear stress, arc plasma shear stress, and arc pressure. Additional source terms described in Eqs. (13) and (17) are added to the energy equation for the special treatment of the anode sheath and the cathode sheath.

A fixed computational domain is used to solve the equations in the arc region. The metal region is used as the inner boundary for the arc region. As the velocity of the metal domain is much smaller than the velocity of the arc plasma, the metal region serves as an inner obstacle in the arc domain. The temperature at the metal free surface is considered as the temperature boundary for the arc domain. Additional source terms described in Eqs. (16) and (18) are added to the energy equation for the arc near the anode and cathode.

III. NUMERICAL CONSIDERATIONS

In the present study, the transport phenomena in the arc plasma and the metal are calculated separately in the corresponding metal domain and arc domain, and the two domains are coupled through interfacial boundary conditions in each time step. The current distribution is greatly influenced by the temperature in the arc column and the shape of the metal domain, but it is only slightly influenced by the temperature distribution in the metal domain as the electrical conductivity of metal varies slightly with temperature. Therefore, the current continuity equation and its associated boundary conditions are solved in the entire domain, while other primary variables, including p, u, v, and T, are calculated separately in the metal domain and the arc domain. The current continuity equation is iterated with the transport equations in the arc domain to obtain the current density distribution for both the arc domain and the metal domain. Iterations are required to assure convergence of each domain and then the boundary conditions are calculated from each domain for the coupling between the two domains.

For the metal domain, the method developed by Torrey *et al.*[32] was used to solve p, u, v, and T. This method is Eulerian and allows for an arbitrary number of segments of free surface with any reasonable shape. The basic procedure for advancing the solution through one time step, Δt, consists of three steps. First, at the beginning of the time step, explicit approximations to the momentum equations [2,3] are used to find provisional values of the new time velocities. Second, an iterative procedure is used to solve for the advanced time pressure and velocity fields that satisfy Eq. (1) to within a convergence criterion at the new time. Third, the energy equation is solved.

For the arc plasma domain, a fully implicit formulation is used for the time-dependent terms, and the combined convection/diffusion coefficients are evaluated using an upwind scheme. The SIMPLE algorithm[33] is applied to solve the momentum and continuity equations to obtain the velocity field. At each time step, the current continuity equation is solved first, based on the updated parameters. Current density and electromagnetic force are then calculated for the momentum and energy equations. The momentum equations

TABLE II. Thermophysical properties of stainless steel and other parameters.

Nomenclature	Symbol	Value (unit)
Constant in Eq. (14)	A_v	2.52
Specific heat of solid phase	c_s	700 (J kg^{-1} K^{-1})
Specific heat of liquid phase	c_l	780 (J kg^{-1} K^{-1})
Thermal conductivity of solid phase	k_s	22 (W m^{-1} K^{-1})
Thermal conductivity of liquid phase	k_l	22 (W m^{-1} K^{-1})
Density of solid phase	ρ_s	7200 (kg m^{-3})
Density of liquid phase	ρ_l	7200 (kg m^{-3})
Thermal expansion coefficient	β_T	4.95×10^{-5} (K^{-1})
Radiation emissivity	ε	0.4
Dynamic viscosity	μ_l	0.006 (kg m^{-1} s^{-1})
Latent heat of fusion	H	2.47×10^{5} (J kg^{-1})
Latent heat of vaporization	H_{ev}	7.34×10^{6} (J kg^{-1})
Solidus temperature	T_s	1750 (K)
Liquidus temperature	T_l	1800 (K)
Vaporization temperature	T_{ev}	3080 (K)
Surface tension coefficient	γ	1.2 (N m^{-1})
Surface tension temperature gradient	$\partial \gamma / \partial T$	10^{-4} (N m^{-1} K^{-1})
Electrical conductivity	σ_e	7.7×10^{5} (Ω^{-1} m^{-1})
Magnetic permeability	μ_0	1.26×10^{-6} (H m^{-1})
Work function	ϕ_w	4.3 (V)
Argon ionization energy	V_i	15.76 (V)

and the continuity equation are then solved in the iteration process to obtain pressure and velocity. The energy equation is solved to get the new temperature distribution. Next, the temperature-dependent parameters are updated, and the program goes back to the first step to calculate the current continuity equation. This process is repeated for each time step until the convergence criteria are satisfied.

The governing differential equations [Eqs. (1)–(5) and (19)] and all related supplemental and boundary conditions are solved through the following iterative scheme.

(1) At $t=0$, the electrode is set up at an initial position and initial temperature distribution is given to the metal domain. Based on the initial fixed metal domain and temperature distribution, the initial distributions of temperature, velocity, pressure, and current are obtained by solving the steady state equations in the arc domain [this procedure is similar to the steps from (5)–(7) for the steady state].

(2) Surface tension, Marangoni shear stress, electromagnetic force, plasma shear stress, and arc pressure are calculated, and other associated boundary conditions are evaluated for the metal domain.

(3) Equations (1)–(4) are solved iteratively to obtain pressure, velocity, and temperature in the metal domain.

(4) VOF, Eq. (19), is solved to obtain the new free surface profile for the metal domain. The physical properties of cells and the boundary conditions within the computing domain are updated.

(5) The current continuity equation (5) is solved in the whole domain with updated parameters. Current density and electromagnetic force are calculated.

(6) Equations (1)–(3) and the associated boundary conditions are solved iteratively to get the velocity and pres-
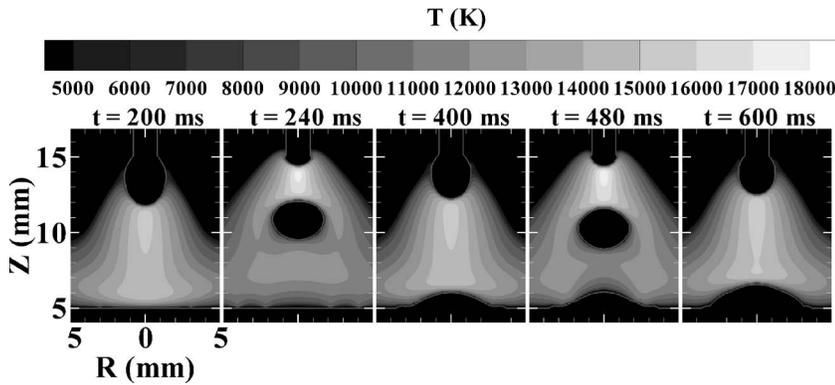
FIG. 3. Temperature distribution for the 175 A constant current.

sure distributions of the arc plasma. When solving these equations, the electrode, the droplet, and the workpiece are treated as fixed inner obstacles.

(7) Energy equation (4) is solved in the arc domain to get the new temperature distribution. Thermal physical properties of the arc plasma are updated. From here, the iteration goes back to step (5) to repeat the process for new distribution of current density, velocity pressure, and temperature, until convergence criteria are satisfied.

(8) Advance to the next time step and back to step (2) until the desired time is reached.

A nonuniform grid system is employed with finer grid sizes near both the cathode and anode regions.

The calculation domain is half of the cylinder of 5.0 cm radius and 3.04 cm in length. Extensive tests have been conducted using different grid sizes and time step sizes to assure consistent results, and the final grid and time step sizes can be considered the compromise between computational time and numerical accuracy. The mesh sizes near the anode and cathode centers are set as 0.01 cm. Time step size is set as 5×10^{-6} s.

IV. RESULTS AND DISCUSSION

The electrode is a stainless steel with a 0.16 cm diameter. The workpiece is also a stainless steel disk with a 3 cm diameter and a 0.5 cm thickness. The imposed external shielding gas flows out of a gas nozzle with a 1.91 cm inner diameter at a rate of 24 l/min. The contact tube is set flush with the bottom of the gas nozzle and is 2.54 cm above the workpiece. The initial arc length is set as 0.8 cm. The temperature-dependent radiation loss term (S_R) in Eq. (4) and

the temperature-dependent material properties of argon, including specific heat, thermal conductivity, electrical conductivity, density, and viscosity, are taken from Ref. 3. The thermophysical properties of the solid and liquid stainless steel are listed in Table II. Five welding currents were studied, including two constant currents and three pulsed currents. The constant currents include one low current at 175 A and one high current at 280 A. Three pulsed currents were studied to investigate the effect of pulse shape and peak duration on droplet detachment. In these three cases, the peak current is set to be 400 A and the average current is 175 A. The peak durations for the three cases are, respectively, 5, 2, and 10 ms. The pulse frequency for the first two cases is 20 Hz and is 25 Hz for the third case. The base currents are, respectively, 150, 165, and 140 A. The wire feed rate selected for 280 A is 7 cm/s, and 4 cm/s for all other cases with an average current of 175 A.

A. Constant current

Figures 3 and 4 show the temperature distributions for the two constant currents at 175 and 280 A. As the temperature of metal is much lower than that of the arc plasma, the metal appears to be dark while the arc plasma has a bright column between the electrode and the workpiece. The surfaces of metal, which include the electrode, droplet, and workpiece, are also marked by the white lines in Figs. 3 and 4.

At a constant current of 175 A, as shown in Fig. 3, a large amount of liquid metal accumulates at the electrode tip before the droplet detaches. After a long droplet formation time, the droplet is detached from the electrode tip with an average diameter of 3.2 mm. The droplet detachment fre-
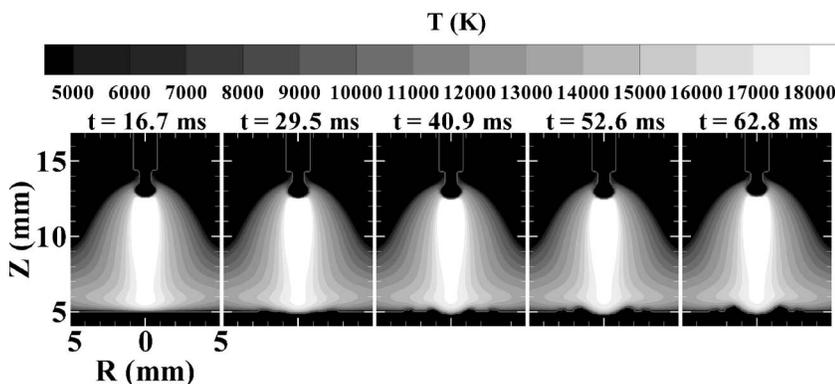

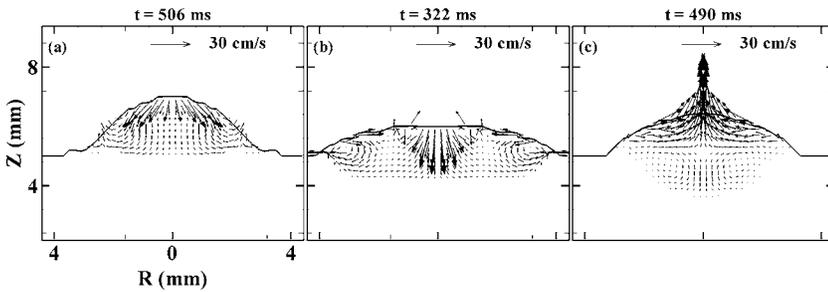FIG. 4. Temperature distribution for the 280 A constant current.

FIG. 5. Velocity distributions in the weld pool for three currents: (a) 175 A, (b) 280 A, and (c) pulsed current with an average current of 175 A.

quency is less than 5 Hz. As the electromagnetic force is small at low currents, the droplet is detached by the competition of surface tension and gravity force. During a real welding process, the big droplet hanging at the electrode tip often wanders around the electrode and suddenly is detached by the surrounding disturbance, causing serious spattering problems at low current levels.

At a high current level, the electromagnetic force plays a major role in pinching the droplet off the electrode tip. The moments near droplet detachment are shown in Fig. 4 for the first five droplets at a high constant current of 280 A. Comparing Fig. 4 with Fig. 3, the arc plasma temperature is higher, the droplet size is smaller, and the droplet formation time is shorter at 280 A than at 175 A. The average diameter of the detached droplets at 280 A is 1.4 mm and the detachment frequency is 90 Hz.

The detached droplets are pushed downward by the arc plasma and accelerated toward the workpiece. The detailed description of the detached droplet transfer process in the arc can be found in Ref. 25. The detached droplet has a higher acceleration under the higher current condition. When the droplet reaches the surface of the workpiece, the average velocity of the droplet is 40 cm/s at 175 A and 110 cm/s at 280 A. The droplet then impinges onto the workpiece, melts part of the workpiece, and forms a weld pool there. Droplet impingement onto the weld pool has a big influence on weld pool shape and penetration depth. As shown in Fig. 3, the weld pool surface underneath the arc plasma has a round shape where there are only four or five droplets per second impinge onto the weld pool with low velocities. While for a higher current of 280 A, the weld pool has a concave shape underneath the arc plasma, where there are frequent high speed droplets impinging onto the weld pool, as shown in Fig. 4. Another reason for the more flattened weld pool at high current is that the arc pressure is higher.

Figure 5 shows some typical weld pool shape and velocity distributions in the weld pool for three different currents. In order to increase the readability, only a quarter of the grid nodes were used in Fig. 5. As the wire feed speed is different for 280 and 175 A, it takes about 322 ms to have the same amount of filler metal deposited into the weld pool for 280 A, while about 506 ms for 175 A. As shown in Fig. 5, the weld pool shape is bigger and flatter and the weld pool depth is bigger for 280 A than for 175 A. Thus, a deeper weld penetration can be achieved with shorter welding time at higher currents. However, a bigger weld pool forms at higher currents, which means a bigger heat-affected zone. Pulsed currents can achieve both a small weld pool and a deep penetration at a low average current. As shown in Fig.

5(c) for a 20 Hz pulsed current with an average current of 175 A, the weld pool is smaller than that for 280 A, and the weld pool penetration is deeper than that for 175 A.

B. Pulsed current

The weld pool shape is greatly related to the droplet size, impingement velocity, and frequency, which cannot be controlled by constant currents, but can be achieved by pulsed currents. By choosing different pulsed current wave forms, the droplet size, impingement velocity, and frequency can be controlled. In this section, simulations of three pulsed currents are carried out to study the effect of peak current duration on droplet transfer.

Figure 6 shows the dynamic droplet development and detachment process of the first case with peak duration of 5 ms. The droplet profiles with current pulses are shown in Fig. 6 for the first two pulses. A round droplet grows during the base duration and is hold onto the electrode tip by surface tension. When a 400 A peak pulse is applied at $t=45$ ms, the droplet is elongated and detached at $t=50.4$ ms. The detached droplet is transferred in the arc to the workpiece while another droplet forms at the electrode tip. No other droplet is detached in the following base duration. Thus, one droplet is detached at the end of peak current for each pulse. The detached droplets have an average diameter of 1.9 mm.

The arc plasma temperature distributions for the first droplet detachment are shown in Fig. 7, in which a much brighter arc plasma can be seen in the peak duration from $t=45$ to 50 ms. As the droplet is detached at the end of the peak duration, the detached droplet is transferred in a low base current during which the acceleration is low. The electromagnetic force distributions for the first droplet detachment are shown in Fig. 8. The corresponding velocity distri-
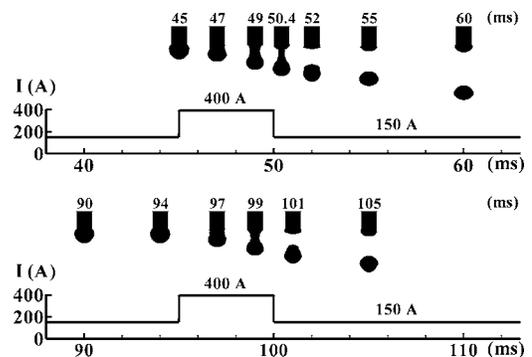

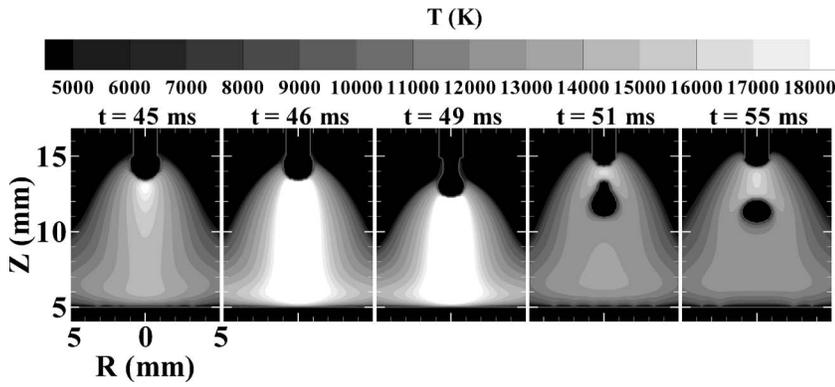FIG. 6. Droplet profiles during the metal transfer process with a pulsed current of 5 ms peak duration.

FIG. 7. Temperature distributions for a pulsed current of 5 ms peak duration.

butions and temperature distributions in the droplet are shown in Figs. 9 and 10, respectively. The pinch effect of electromagnetic force is the deterministic factor for droplet detachment in this case. The magnitude of electromagnetic force in the metal at base current is 10^6 N/m^3, as shown at $t=45$ ms in Fig. 8, which is small and a round droplet forms stably at the electrode tip. As seen in Fig. 9, a counterclockwise flow exists in the droplet where surface tension is the dominant force. From Figs. 9 and 10, it can be seen that a counterclockwise flow brings the cool liquid metal at the droplet root downward and the hot liquid at the droplet surface to the upper part of the droplet. Then, at $t=46$ ms, the electromagnetic force increases to 10^7 N/m^3 in peak duration. The greatly increased electromagnetic force pinches the liquid metal in the droplet and accelerates it downward. At $t=46$ ms, the downward velocity of the liquid metal in the droplet is much higher than at $t=45$ ms and the counterclockwise flow pattern inside the droplet is not obvious.

The liquid metal quickly moves downward and a neck already forms at $t=48$ ms. After a neck forms, the electromagnetic force significantly increases its magnitude and changes its distribution within the liquid metal. Above the waist of the droplet, the electromagnetic force has inward

and downward directions and squeezes the liquid metal to flow inward and upward. Below the waist, it has inward and downward directions and pinches the liquid metal to flow downward. This motion helps to elongate and narrow the droplet neck and further increase the electromagnetic force. Thus, once a neck forms, the droplet is detached very quickly. After a neck forms at $t=48$ ms, there is no hot liquid brought up to the upper part of the droplet by the counterclockwise flow at the droplet surface. However, a counterclockwise vortex forms above the droplet waist which is due to the pinch effect of electromagnetic force on the upper part of the liquid metal. The change of flow pattern inside the droplet changes the temperature distribution within the droplet. As shown in Fig. 10, the concave melting surface at the droplet root becomes flat and then convex after a neck forms. After a droplet detaches, the remaining liquid at the electrode tip is bounced back and forms another droplet at the low base current.

Peak duration is very important to form one droplet per pulse. As it is shown in Fig. 11, the 2 ms peak duration is insufficient to detach the droplet from the electrode tip and the subsequent current pulse also fails to detach the growing
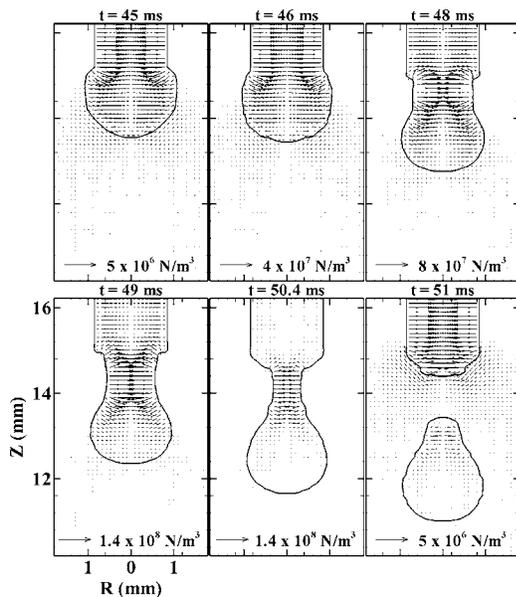

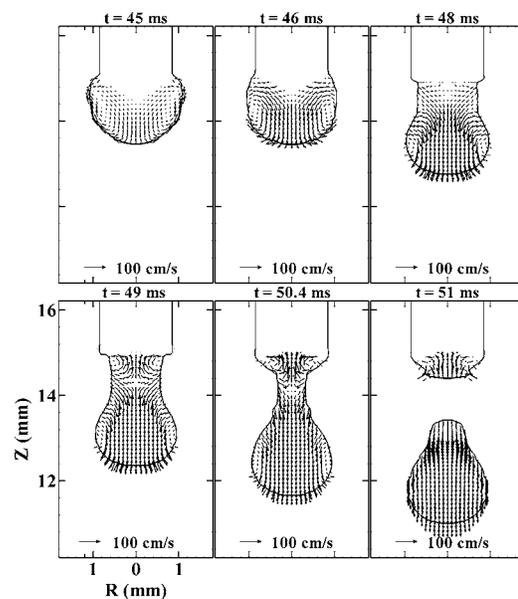FIG. 8. Electromagnetic force distributions for a pulsed current of 5 ms peak duration.

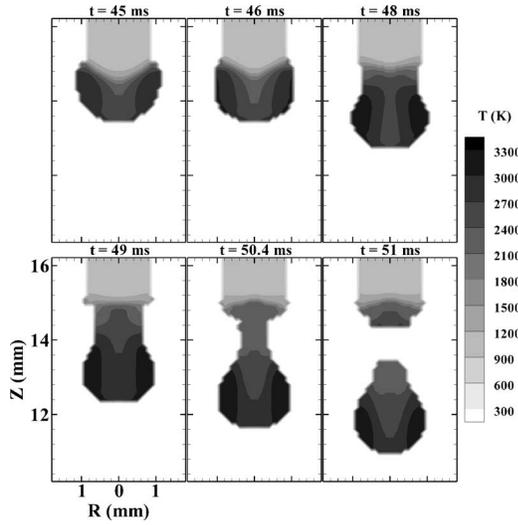FIG. 9. Velocity distributions for a pulsed current of 5 ms peak duration.

FIG. 10. Temperature distributions for a pulsed current of 5 ms peak duration.

FIG. 12. Electromagnetic force distributions for a pulsed current of 2 ms peak duration.

droplet. The distributions of electromagnetic force and velocity for the first pulse are shown in Figs. 12 and 13, respectively.

From $t=48$ to 50 ms, the increased electromagnetic force in the peak duration elongates the droplet and accelerates the liquid metal to flow downward. After current returns to the base level at $t=50$ ms, the liquid metal in the droplet continues to flow downward by inertia and a neck forms at the droplet root. As the neck area is still big and the electromagnetic is still small at the base current, the small electromagnetic force cannot overcome the resistance of surface tension force and pinch the droplet off from the electrode tip. The liquid metal in the droplet continues to flow downward, but downward velocity decreases after the electromagnetic force becomes smaller. The elongated shape of droplet causes a big surface tension force, which helps the droplet rebound back to the electrode tip. As shown in Fig. 11, after a few cycles of oscillation, the droplet is stabilized and grows larger at the electrode tip till the second pulse is applied. The increased electromagnetic force during the second pulse peak duration pinched the liquid metal to flow downward from $t=100$ ms. However, the pinch effect is even smaller on the liquid metal as the droplet becomes bigger now than in the first pulse. The second pulse also fails to
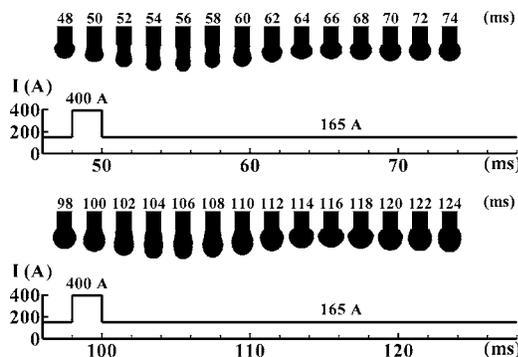
detach the droplet, and the droplet grows big at the electrode tip till it grows too big that surface tension cannot hold it onto to the electrode.

If the peak duration is too long, the undesirable multiple droplets per pulse occurs. As shown in Fig. 14, three droplets are detached in each pulse for peak duration of 10 ms (note some droplets are shown partially). After a droplet is detached, the remaining fluid is pinched off by the high electromagnetic force with a form of two subsequent small droplets. The detailed process is shown with the corresponding distributions of electromagnetic force and velocity in Figs. 15 and 16. It should be noted that the detached droplets were removed from Fig. 15 for readability. After the first droplet is pinched off at $t=66$ ms by the increased electromagnetic force, the electromagnetic force is still high as it is still in the

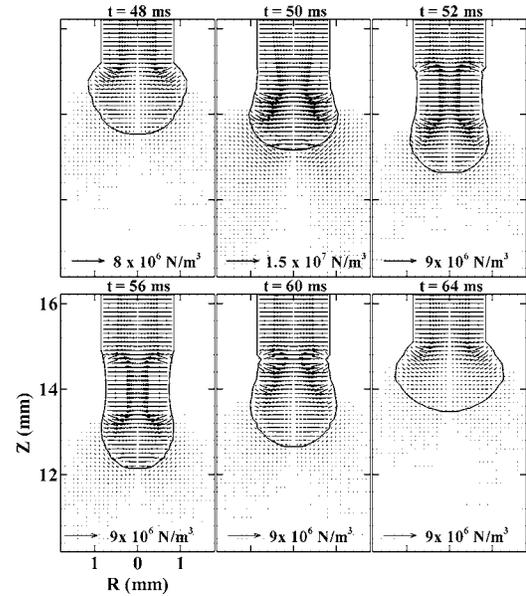FIG. 11. Droplet profiles during the metal transfer process with a pulsed current of 2 ms peak duration.
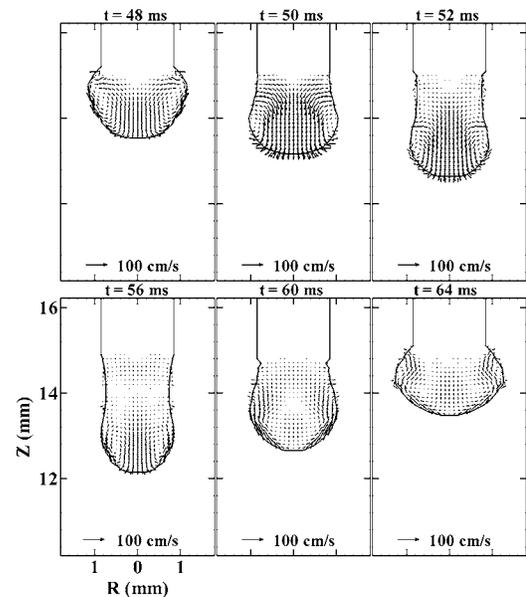

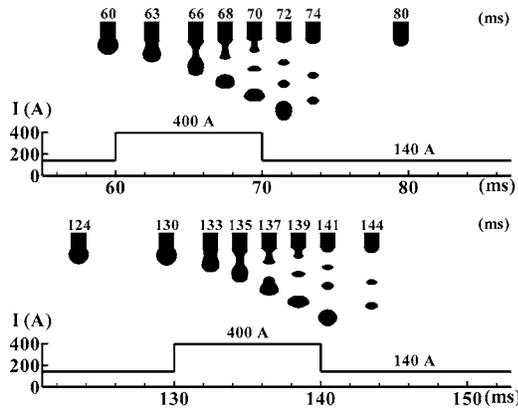FIG. 13. Velocity distributions for a pulsed current of 2 ms peak duration.

FIG. 14. Droplet profiles during the metal transfer process with a pulsed current of 10 ms peak duration.

peak duration. The remaining fluid at the electrode tip after the detachment of the first droplet is pinched to form a liquid column by the high electromagnetic force. Due to the small volume of liquid and very high electromagnetic pinch force in the small necking area, two small droplets are detached within 4 ms. After the current changes back to the base current at $t=70$ ms, the remaining liquid at the electrode tip was bounced back by the surface tension and also the upward motion of the liquid and another big droplet forms stably at the base current.

V. CONCLUSIONS

Using the comprehensive model, this paper has studied the effects of welding current on the droplet generation, metal transfer, and weld pool dynamics. Five cases are studied, including two different levels of constant currents and three pulsed currents with different peak durations. The results showed that a higher electromagnetic force was generated at a higher current and becomes the dominant factor that detaches the droplet from the electrode tip. A smaller droplet
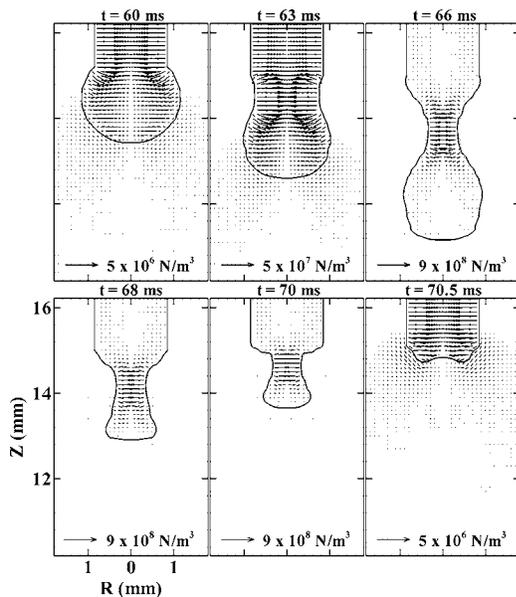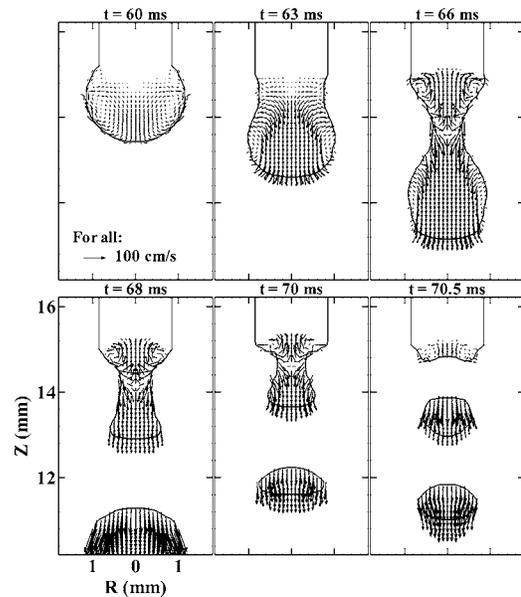

FIG. 16. Velocity distributions for a pulsed current of 10 ms peak duration.

size and a higher droplet frequency were obtained for a higher current. It was also found that for constant welding current, the higher the current, the deeper the penetration, and the bigger the weld pool; while for pulsed current, the weld pool shape and penetration can be controlled by controlling droplet size, frequency, and velocity through pulse shape. The peak duration was also studied to show that a stable ODPP transfer mode can be achieved by carefully choosing peak duration, which has demonstrated that a stable ODPP metal transfer mode can be achieved by choosing a current with proper wave form for given welding conditions.

ACKNOWLEDGMENT

[1] S. T. Eickhoff and T. W. Eagar, Weld. J. (Miami, FL, U.S.) **69**, 382s (1990).
[2] A. Lesnewich, Weld. J. (Miami, FL, U.S.) **37**, 343s (1958).
[3] J. F. Lancaster, *The Physics of Welding*, 2nd ed. (Pergamon, Oxford, 1986).
[4] W. J. Greene, Am. Inst. Electr. Eng. **79**, 194 (1960).
[5] J. C. Amson, Br. J. Appl. Phys. **16**, 1169 (1965).
[6] L. A. Jones, T. W. Eagar, and J. H. Lang, J. Phys. D **31**, 107 (1998).
[7] C. J. Allum, J. Phys. D **18**, 1431 (1985).
[8] C. J. Allum, J. Phys. D **18**, 1447 (1985).
[9] J. Haidar and J. J. Lowke, J. Phys. D **29**, 2951 (1996).
[10] J. Haidar, J. Appl. Phys. **84**, 3530 (1998).
[11] S. K. Choi, C. D. Yoo, and Y.-S. Kim, J. Phys. D **31**, 207 (1998).
[12] S. K. Choi, C. D. Yoo, and Y.-S. Kim, Weld. J. (Miami, FL, U.S.) **77**, 38s (1998).
[13] F. Wang, W. K. Hou, S. J. Hu, E. Kannatey-Asibu, W. W. Schultz, and P. C. Wang, J. Phys. D **36**, 1143 (2003).
[14] H. G. Fan and R. Kovacevic, J. Phys. D **31**, 2929 (1998).
[15] F. L. Zhu, H. L. Tsai, S. P. Marin, and P. C. Wang, Prog. Comput. Fluid Dyn. **4**, 99 (2004).
[16] H. G. Fan and R. Kovacevic, J. Phys. D **37**, 2531 (2004).
[17] G. Wang, P. G. Huang, and Y. M. Zhang, Metall. Mater. Trans. B **35B**, 857 (2004).
[18] Q. Z. Diao and H. L. Tsai, Metall. Trans. A **24A**, 963 (1993).
[19] P. C. Carman, Trans. Inst. Chem. Eng. **15**, 150 (1937).

FIG. 15. Electromagnetic force distributions for a pulsed current of 10 ms peak duration.

[20] K. Kubo and R. D. Pehlke, Metall. Trans. A **16A**, 823 (1985).
[21] G. S. Beavers and E. M. Sparrow, J. Appl. Mech. **36**, 711 (1969).
[22] J. J. Lowke, P. Kovitya, and H. P. Schmidt, J. Phys. D **25**, 1600 (1992).
[23] W. Simpson and P. Y. Zhu, J. Phys. D **28**, 1594 (1995).
[24] J. Haidar, J. Phys. D **31**, 1233 (1998).
[25] J. Hu, Ph.D. thesis, University of Missouri-Rolla, 2005.
[26] J. Haidar, J. Appl. Phys. **84**, 3518 (1998).
[27] W. Finkelnburg and S. M. Segal, Phys. Rev. Lett. **83**, 582 (1951).
[28] T. Zacharia, S. A. David, and J. M. Vitek, Metall. Trans. B **22B**, 233 (1992).
[29] P. G. Jonsson, R. C. Westhoff, and J. Szekely, J. Appl. Phys. **74**, 5997 (1993).
[30] J. U. Brackbill, D. B. Kothe, and C. Zemach, J. Comput. Phys. **100**, 335 (1992).
[31] R. A. Granger, *Fluid Mechanics* (CBS College, New York, 1985), Chap. 10.
[32] M. D. Torrey, L. D. Cloutman, R. C. Mjolsness, and C. W. Hirt, Los Alamos Report No. LA-10612-MS, 1985.
[33] S. V. Patanka, *Numerical Heat Transfer and Fluid Flow* (McGraw-Hill, New York, 1980).